ELSEVIER

Engineering Analysis with Boundary Elements 29 (2005) 1025–1038

ENGINEERING ANALYSIS *with* BOUNDARY ELEMENTS

www.elsevier.com/locate/enganabound

A time-domain collocation-Galerkin BEM for transient dynamic crack analysis in anisotropic solids

A. Tan [a], S. Hirose [b,*], Ch. Zhang [c]

[a] *Department of Civil Engineering, Tokyo Institute of Technology, Tokyo 152-8552, Japan*
[b] *Department of Mechanical and Environmental Informatics, Tokyo Institute of Technology, Tokyo 152-8552, Japan*
[c] *Department of Civil Engineering, University of Siegen, D-57068 Siegen, Germany*

Received 16 December 2004; accepted 9 May 2005
Available online 29 September 2005

Abstract

This paper presents a time-domain boundary element method (BEM) for transient elastodynamic crack analysis in homogeneous and linear elastic solids of general anisotropy. A finite crack subjected to a transient loading is investigated. Two-dimensional (2D) generalized plane-strain or plane-stress condition is considered. The initial-boundary value problem is described by a set of hypersingular time-dependent traction boundary integral equations (BIEs), in which the crack-opening displacements (CODs) are unknown quantities. The hypersingular time-domain BIEs are first regularized to weakly singular ones by using spatial Galerkin method, which transfers the derivatives of the fundamental solutions to the unknown CODs and the weight functions. To solve the time-domain BIEs numerically, a time-stepping scheme is developed. The scheme applies the collocation method for temporal discretization of the time-domain BIEs. As spatial shape-functions, two different functions are implemented. For elements away from crack-tips, linear spatial shape-function is used, while for elements near the crack-tips a special 'crack-tip shape-function' is applied to describe the local 'square-root' behavior of the CODs at the crack-tips properly. Special attention of the analysis is devoted to the numerical computation of the transient elastodynamic stress intensity factors for cracks in general anisotropic and linear elastic solids. Numerical examples are presented to verify the accuracy of the present time-domain BEM.

Keywords: Time-domain BEM; Collocation method; Galerkin-method; Anisotropioc solids; Transient dynamic crack analysis; Stress intensity factors

1. Introduction

In linear elastic fracture mechanics, the most important crack-tip characterizing parameters are the stress intensity factors, and they represent the strength of the square-root singularity of the stress and the strain fields at the crack-tips. Once the size, the location and orientation of a crack has been characterized, stress intensity factors can be used to assess the initiation, the propagation and the arrest of an existing crack.

Due to the important role of the stress intensity factors in linear elastic fracture mechanics, their analytical, numerical or experimental determination in cracked solids is a key issue in linear elastic fracture mechanics. Since analytical solutions can be obtained only for very simple crack geometry and loading configurations, numerical methods are often used. For homogeneous, isotropic and linear elastic solids with cracks subjected to static or dynamic loading conditions, the boundary integral equation method (BIEM) or the boundary element method (BEM) has proven to be very accurate and efficient for this purpose [5,7]. For homogeneous, anisotropic and linear elastic solids, the BIEM or BEM has also been successfully applied to elastostatic crack analysis, although the corresponding elastostatic fundamental solutions or Green's functions in anisotropic case are much more complicated than the isotropic counterpart [5,9,10,12,16,18,19,23,24,36]. In contrast, developments and applications of the BEM to dynamic crack analysis in anisotropic and linear elastic solids are yet still very limited, because the elastodynamic fundamental solutions for general anisotropic solids are mathematically very complicated and cannot be expressed in explicit and simple forms. The complicated form of the elastodynamic fundamental solutions for anisotropic solids makes the numerical implementation of the BIEM/BEM cumbersome and may affect the efficiency of the BIEM/BEM.

Though different BIEM/BEM formulations can be found in literature for transient elastodynamic crack analysis in

* Corresponding author. Tel.:/fax: +81 3 5734 2692.
E-mail address: shirose@cv.titech.ac.jp (S. Hirose).

0955-7997/$ - see front matter © 2005 Elsevier Ltd. All rights reserved.
doi:10.1016/j.enganabound.2005.05.009

homogeneous, anisotropic and linear elastic solids, they can be divided into the following cases:

- *Dual reciprocity BEM using elastostatic fundamental solutions* [2–4]. This method avoids the use of the complex elastodynamic fundamental solutions for anisotropic solids, and applies the corresponding elastostatic fundamental solutions. In this method, certain interior nodes are needed to describe the inertial effects accurately.
- *Time-domain BEM using time-domain elastodynamic fundamental solutions* [29,13–15,25]. A time-domain displacement BEM for transient wave scattering analysis by cavities has been developed by Wang et al. [29]. The method uses the time-domain elastodynamic fundamental solutions for anisotropic solids, which have been derived by Wang and Achenbach [28] by using Randon-transform. Later, the time-domain displacement BEM has been extended to transient crack analysis in anisotropic solids, where the traction BIEs have been applied [13–15,25].
- *Time-domain BEM using Laplace-domain elastodynamic fundamental solutions* [33–35]. This method uses the same set of the time-domain traction BIEs as in the conventional formulation, but utilizes the Laplace-transformed instead of the time-dependent elastodynamic fundamental solutions. This can be realized by using the convolution quadrature formula. A comparison of both time-domain BEMs has been given by Hirose et al. [15].
- *Frequency-domain BEM using time-harmonic elastodynamic fundamental solutions* [11,20]. In this method, hypersingular traction BIEs are formulated in the frequency-domain by using time-harmonic elastodynamic fundamental solutions. After the corresponding boundary value problem has been solved numerically for discrete frequencies, transient dynamic solutions can be obtained by the inverse Fourier-transform. The same procedure can be applied to the Laplace-domain BEM, where the Laplace-transformed elastodynamic fundamental solutions and an inverse Laplace-transform have to be used.

This paper presents a two-dimensional (2D) time-domain collocation-Galerkin BEM for transient elastodynamic crack analysis in homogeneous, anisotropic and linear elastic solids. An infinite, homogeneous, anisotropic and linear elastic solid containing a finite crack is considered. The cracked solid is subjected to transient incident wave loading, and 2D generalized plane-strain or plane-stress condition is assumed. To solve the resulting initial-boundary value problem, hypersingular time-domain traction BIEs are applied, in which the crack-opening-displacements (CODs) are the fundamental unknown quantities. The hypersingular integrals are understood in the sense of Hadamard finite-part integrals. To solve the time-domain traction BIEs, a time-stepping scheme is developed. The scheme uses the time-domain elastodynamic fundamental solutions derived by Wang and Achenbach [28]. Collocation method is adopted to approximate the time-convolution integral, while Galerkin-method is utilized for the spatial discretization of the time-domain BIEs. By using linear temporal shape function, the convolution integrals can be integrated analytically. For the spatial approximation of the CODs, two different spatial shape functions are applied. For elements away from the crack-tips, standard linear elements are adopted, while at the crack-tips the so-called 'crack-tip elements' are introduced to describe the local square-root behavior of the CODs properly. Since the elastodynamic fundamental solutions can be split into a static and a dynamic part, the system matrix can also be divided into a static and a dynamic system matrix. The hypersingular integrals arise only in the static system matrix, and they are regularized into weakly singular integrals before the integration is carried out. For linear elements, spatial integrations can be performed analytically for both static and dynamic system matrices. In the case of the 'crack-tip elements', spatial integrations are carried out analytically and numerically. The integral over the unit circle arising in the dynamic part of the fundamental solutions is done numerically. After the CODs have been obtained numerically, the elastodynamic stress intensity factors can be obtained immediately. The use of the 'crack-tip elements' ensures an accurate numerical calculation of the dynamic stress intensity factors. Several numerical examples are given to demonstrate the accuracy and the efficiency of the present time-domain collocation-Galerkin BEM.

2. Formulation of the initial boundary-value problem

We consider a two-dimensional (2D), infinite, linearly elastic and anisotropic solid containing a finite crack of arbitrary shape as shown in Fig. 1. Without body forces, the cracked solid satisfies the equations of motion [1]

$$\sigma_{i\beta,\beta} = \rho \ddot{u}_i, \tag{1}$$

and the Hooke's law

$$\sigma_{i\beta} = C_{i\beta k\lambda} u_{k,\lambda}, \tag{2}$$

where u_i and $\sigma_{i\beta}$ are the displacement and the stress components, ρ is the mass density and $C_{i\beta k\lambda}$ are the components of the fourth–order elasticity tensor. A comma after a quantity denotes partial derivative with respect to the spatial variables, and the conventional summation rule over repeated indices is applied throughout this paper. Also, Roman suffixes take values of 1, 2 and 3 while Greek suffixes have values of 1 and 2 only. Substitution of Eq. (2) into Eq. (1) results in the following equations of motion for the displacement components

$$[\Gamma_{ij}(\partial_1, \partial_2) - \rho\delta_{ij}\partial_t^2]u_j(x,t) = 0, \tag{3}$$

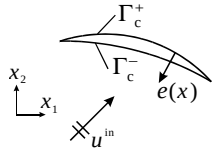

Fig. 1. A finite crack in an infinite anisotropic solid.

where

$$\Gamma_{ij}(\partial_1,\partial_2) = C_{i\alpha j\beta}\partial_\alpha\partial_\beta, \tag{4}$$

is the second-order Christoffel tensor, and ∂_α represents partial derivative with respect to a spatial variable x_α. It should be noted here that although the displacement and the stress fields in a 2D analysis are independent of the x_3-coordinate, the in-plane and the anti-plane deformations are generally not decoupled in anisotropic solids.

An incident elastic wave interacts with the crack which induces scattered waves. Hence, the total wave field can be written as

$$u_i = u_i^{\text{in}} + u_i^{\text{sc}}, \quad t_i = t_i^{\text{in}} + t_i^{\text{sc}}, \tag{5}$$

where $t_i = \sigma_{i\beta}e_\beta$ denotes the traction vector with $\mathbf{e}_\beta$ being the outward unit normal vector to the crack-faces. Throughout the analysis, the superscript "in" denotes the incident wave field, while "sc" stands for the scattered wave field.

The following initial conditions are assumed

$$u_i(\mathbf{x},t) = \dot{u}_i(\mathbf{x},t) = 0, \quad t = 0. \tag{6}$$

Furthermore, traction-free boundary conditions on the crack-faces are considered, i.e.

$$t_i(\mathbf{x},t) = \sigma_{i\beta}(\mathbf{x},t)e_\beta(\mathbf{x}) = 0, \quad \mathbf{x}\in\Gamma_{\text{c}}, \tag{7}$$

in which $\Gamma_{\text{c}} = \Gamma_{\text{c}}^+ + \Gamma_{\text{c}}^-$ represents the crack-faces with Γ_{c}^+ and Γ_{c}^- being the upper and the lower one.

Eqs. (3)–(7) form the initial-boundary value problem for transient elastodynamic crack analysis in anisotropic and linear elastic solids. In this analysis, the incident wave fields are assumed to be given, while the scattered wave fields have to be determined by solving the above stated initial-boundary value problem. To this end, a time-domain boundary integral equation formulation is applied, which is presented in the following sections.

3. Time-domain elastodynamic fundamental solutions

The dynamic fundamental solutions or Green's functions are solutions of the following partial differential equations

$$[\Gamma_{ki}(\partial_1,\partial_2) - \rho\delta_{ki}\partial_t^2]g_{ij}(\mathbf{x},\mathbf{y};t) = -\delta_{kj}\delta(\mathbf{x}-\mathbf{y})\delta(t), \tag{8}$$

with initial conditions

$$g_{ij}(\mathbf{x},\mathbf{y};t) = 0, \quad \text{for} \quad t\le 0. \tag{9}$$

By applying the Radon transform to Eqs. (8) and (9), Wang and Achenbach obtained the following displacement fundamental solution [28]

$$g_{ij}(\mathbf{x},\mathbf{y};t) = \frac{H(t)}{4\pi^2}\int_{|\mathbf{n}|=1}\int_{l=1}^{L}\frac{P_{ij}^l}{\rho c_l}\left(\frac{1}{c_l t + \mathbf{n}\cdot(\mathbf{x}-\mathbf{y})}\right)\mathrm{d}\mathbf{n}, \tag{10}$$

where $P_{ij}^l = E_{il}E_{jl}$ is the projection operator, while E_{ij} and ρc_l^2 are the eigenvectors and the eigenvalues of the matrix,

$$\Gamma_{ik}(n_1,n_2) = C_{i\alpha k\beta}n_\alpha n_\beta, \tag{11}$$

in which $\mathbf{n}$ denotes the unit vector of wave propagation. The dynamic displacement fundamental solution can be split into a static part $g_{ij}^{\text{s}}(\mathbf{x},\mathbf{y})$ and a dynamic part $g_{ij}^{\text{d}}(\mathbf{x},\mathbf{y};t)$ as

$$\begin{aligned} g_{ij}(\mathbf{x},\mathbf{y};t)*f(t) &= \frac{1}{4\pi^2}\int_{|\mathbf{n}|=1}\sum_{l=1}^{L}\frac{P_{ij}^l}{\rho c_l^2}\left\{\int_0^t\frac{\partial}{\partial\tau}\log[c_l\tau \right.\\ &\quad \left. + \mathbf{n}\cdot(\mathbf{x}-\mathbf{y})]f(t-\tau)\mathrm{d}\tau\right\}\mathrm{d}\mathbf{n}\\ &= \frac{1}{4\pi^2}\int_{|\mathbf{n}|=1}\sum_{l=1}^{L}\frac{P_{ij}^l}{\rho c_l^2}\{-\log[\mathbf{n}\cdot(\mathbf{x}-\mathbf{y})]f(t)\\ &\quad + \int_0^t\log[c_l\tau + \mathbf{n}\cdot(\mathbf{x}-\mathbf{y})]\dot{f}(t-\tau)\mathrm{d}\tau\Big\}\mathrm{d}\mathbf{n}\\ &= g_{ij}^{\text{s}}(\mathbf{x},\mathbf{y})f(t) + g_{ij}^{\text{d}}(\mathbf{x},\mathbf{y};t)*\dot{f}(t), \end{aligned} \tag{12}$$

where

$$g_{ij}^{\text{s}}(\mathbf{x},\mathbf{y}) = -\frac{1}{4\pi^2}\int_{|\mathbf{n}|=1}\sum_{l=1}^{L}\frac{P_{ij}^l}{\rho c_l^2}\log[\mathbf{n}\cdot(\mathbf{x}-\mathbf{y})], \tag{13}$$

$$g_{ij}^{\text{d}}(\mathbf{x},\mathbf{y};t) = \frac{H(t)}{4\pi^2}\int_{|\mathbf{n}|=1}\int_{l=1}^{L}\frac{P_{ij}^l}{\rho c_l^2}\log[c_l t + \mathbf{n}(\mathbf{x}-\mathbf{y})]\mathrm{d}\mathbf{n}. \tag{14}$$

By applying a variable change and the residue theorem to Eq. (13), an explicit expression for the static displacement fundamental solution can be obtained as [8,30]

$$g_{ij}^{\text{s}}(\mathbf{x},\mathbf{y}) = \frac{1}{\pi}\mathrm{Im}\int_{l=1}^{L}\frac{A_{ij}(\eta_l)}{\partial_\eta D(\eta_l)}\log(z_l) + \alpha_{ij}, \tag{15}$$

where

$$A_{ij}(\eta) = \mathrm{adj}[\Gamma_{ij}(1,\eta)], \qquad D(\eta) = \det[\Gamma_{ij}(1,\eta)], \tag{16}$$

$$z_l = x_1 - y_1 + \eta_l(x_2 - y_2), \qquad l = 1,2,3, \tag{17}$$

$$\begin{aligned} \alpha_{ij} &= -\frac{1}{4\pi^2}\int_{|\mathbf{n}|=1}\Gamma_{ij}^{-1}(\mathbf{n})\log|n_1|\mathrm{d}\mathbf{n}\\ &= -\frac{1}{\pi}\mathrm{Im}\int_{l=1}^{L}\frac{A_{ij}(\eta_l)}{\partial_\eta D(\eta_l)}\log(\eta_l + i). \end{aligned} \tag{18}$$

In Eq. (15), η_l are distinct roots of the characteristic equation

$$D(\eta_l) = 0, \quad \mathrm{Im}(\eta_l) > 0, \quad l = 1,2,3. \tag{19}$$

Since $\Gamma_{ij}(1,\eta)$ is real, symmetric and positive definite, its determinant can never be zero unless η is complex. It is remarked here that the constant term α_{ij} in the static fundamental solution (15) is necessary to maintain the quiescent field ahead of the wave fronts generated by a point force. For a pure static analysis, this term is inessential and should be omitted.

Substitution of Eq. (10) into

$$h_{ik}(\mathbf{x},\mathbf{y};t) = C_{i\alpha j\beta} e_\alpha(\mathbf{x}) g_{jk,\beta}(\mathbf{x},\mathbf{y};t) \tag{20}$$

yields the time-domain traction fundamental solution as

$$h_{ij}(\mathbf{x},\mathbf{y};t) = \frac{H(t)}{4\pi^2} \int_{|\mathbf{n}|=1} \sum_{l=1}^{L} \frac{Q_{ij}^l}{\rho c_l^2} \frac{\partial}{\partial t} \left(\frac{1}{c_l t + \mathbf{n}\cdot(\mathbf{x}-\mathbf{y})} \right) \mathrm{d}\mathbf{n}, \tag{21}$$

in which

$$Q_{ij}^l = C_{i\alpha k\beta} e_\alpha(\mathbf{x}) n_\beta P_{kj}^l(\mathbf{n}). \tag{22}$$

Similarly, by substituting the displacement fundamental solution (10) into

$$w_{ij}(\mathbf{x},\mathbf{y};t) = C_{i\gamma p\delta} C_{j\alpha k\beta} e_\gamma(\mathbf{x}) e_\alpha(\mathbf{y}) \frac{\partial^2 g_{pk}(\mathbf{x},\mathbf{y};t)}{\partial x_\delta \partial y_\beta}, \tag{23}$$

we obtain the following higher-order traction fundamental solution

$$w_{ij}(\mathbf{x},\mathbf{y};t) = -\frac{H(t)}{4\pi^2} \int_{|\mathbf{n}|=1} \sum_{l=1}^{L} \frac{R_{ij}^l}{\rho c_l^3} \frac{\partial^2}{\partial t^2} \left(\frac{1}{c_l t + \mathbf{n}\cdot(\mathbf{x}-\mathbf{y})} \right) \mathrm{d}\mathbf{n} \tag{24}$$

where the derivatives with respect to the spatial variable are transformed into time derivatives, and

$$R_{ij}^l = C_{i\gamma p\delta} C_{j\alpha k\beta} n_\delta n_\beta e_\gamma(\mathbf{x}) e_\alpha(\mathbf{y}) P_{pk}^l(\mathbf{n}). \tag{25}$$

Like the displacement fundamental solution, the traction and the higher-order traction fundamental solutions can also be divided into their static and dynamic parts. For the sake of brevity, we only give the derivation for the higher-order traction fundamental solution in the following. For this purpose, let us consider the following time convolution

$$w_{ij}(\mathbf{x},\mathbf{y};t) * f(t) = -\frac{1}{4\pi^2} \int_{|\mathbf{n}|=1} \sum_{l=1}^{L} \frac{R_{ij}^l}{\rho c_l^3} \left[\int_0^t \frac{\partial^2}{\partial \tau^2} \left(\frac{1}{c_l \tau + \mathbf{n}\cdot(\mathbf{x}-\mathbf{y})} \right) f(t-\tau)\mathrm{d}\tau \right] \mathrm{d}\mathbf{n}. \tag{26}$$

Integrating Eq. (26) by parts twice with respect to time τ we obtain

$$\begin{aligned} w_{ij}(\mathbf{x},\mathbf{y};t) * f(t) &= -\frac{1}{4\pi^2} \int_{|\mathbf{n}|=1} \sum_{l=1}^{L} \frac{R_{ij}^l}{\rho c_l^3} \left[\frac{c_l}{(\mathbf{n}\cdot(\mathbf{x}-\mathbf{y}))^2} f(t) \right. \\ &\quad \left. + \int_0^t \frac{1}{c_l \tau + \mathbf{n}\cdot(\mathbf{x}-\mathbf{y})} \ddot{f}(t-\tau)\mathrm{d}\tau \right] \mathrm{d}\mathbf{n} \\ &= w_{ij}^{\mathrm{s}}(\mathbf{x},\mathbf{y}) f(t) + w_{ij}^{\mathrm{d}}(\mathbf{x},\mathbf{y};t) * \ddot{f}(t), \end{aligned} \tag{27}$$

where

$$w_{ij}^{\mathrm{s}}(\mathbf{x},\mathbf{y}) = -\frac{1}{4\pi^2} \int_{|\mathbf{n}|=1} \sum_{l=1}^{L} \frac{R_{ij}^l}{\rho c_l^2} \frac{1}{(\mathbf{n}\cdot(\mathbf{x}-\mathbf{y}))^2} \mathrm{d}\mathbf{n}, \tag{28}$$

$$w_{ij}^{\mathrm{d}}(\mathbf{x},\mathbf{y};t) = -\frac{H(t)}{4\pi^2} \int_{|\mathbf{n}|=1} \sum_{l=1}^{L} \frac{R_{ij}^l}{\rho c_l^3} \frac{1}{c_l t + \mathbf{n}\cdot(\mathbf{x}-\mathbf{y})} \mathrm{d}\mathbf{n}. \tag{29}$$

Eq. (27) implies that the higher-order traction fundamental solution can be split into a static part and a dynamic part. The static part corresponds to the elastostatic fundamental solution and has a hypersingularity. In contrast, the dynamic part is regular except at the wave front $c_l t + \mathbf{n}\cdot\mathbf{x} = 0$.

As in the case of the static displacement fundamental solution, the higher-order static traction fundamental solution can also be reduced to an explicit expression by applying the Stroh's formalism. By substituting Eq. (15) into Eq. (23) and then applying the Stroh's formalism twice, one obtains [13]

$$w_{ij}^{\mathrm{s}}(\mathbf{x},\mathbf{y}) = \frac{1}{\pi} \frac{\partial}{\partial s_x} \frac{\partial}{\partial s_y} \mathrm{Im} \int_{l=1}^{L} B_{ij}^l(\eta_l) \log[\mathbf{d}_l(\mathbf{x}-\mathbf{y})], \tag{30}$$

in which $\frac{\partial}{\partial S_x}$ indicates the tangential derivative at the point $\mathbf{x}$ and

$$B_{ij}^l(\eta_l) = \frac{(M_{ip} + L_{ip}\eta_l) A_{pk}(\eta_l) (M_{jk} + L_{jk}\eta_l)}{\partial D(\eta_l)}, \quad \mathbf{d}_l = (1, \eta_l). \tag{31}$$

In Eq. (31), L_{ij} and M_{ij} are defined by the following equation

$$\Gamma_{ij}(1,\eta) = L_{ij}\eta^2 + (M_{ij} + M_{ij}^T)\eta + N_{ij}, \tag{32}$$

where

$$N_{ij} = C_{i1j1}, \qquad M_{ij} = C_{i1j2}, \qquad L_{ij} = C_{i2j2}. \tag{33}$$

In passing, it should be remarked again that the higher-order static traction fundamental solution has a hypersingularity at $\mathbf{x}=\mathbf{y}$ as can be seen from Eq. (30).

4. Time-domain boundary integral equations

By using the Betti–Rayleigh reciprocal theorem, a representation integral for the displacement components can be obtained as [1]

$$u_k(\mathbf{y},t) = u_k^{\mathrm{in}}(\mathbf{y},t) - \int_{\Gamma_{\mathrm{c}}^+} h_{ik}(\mathbf{x},\mathbf{y};t) * \Delta u_i(\mathbf{x},t)\mathrm{d}s_x, \quad \mathbf{y} \notin \Gamma_{\mathrm{c}}^+, \tag{34}$$

where $\mathbf{x}$ and $\mathbf{y}$ are the source and the observation points, $h_{ik}(\mathbf{x},\mathbf{y};t)$ is the time-domain elastodynamic traction fundamental solution given by Eq. (20), an * stands for Riemann

convolution

$$g(\mathbf{x},t)*h(\mathbf{x},t)=\int_0^t g(\mathbf{x},t-\tau)h(\mathbf{x},\tau)\mathrm{d}\tau, \tag{35}$$

and $\Delta u_i(\mathbf{x},t)$ are the crack-opening-displacements (CODs) defined by

$$\Delta u_i(\mathbf{x},t)=u_i(\mathbf{x}\in\Gamma_c^+,t)-u_i(\mathbf{x}\in\Gamma_c^-,t). \tag{36}$$

A direct limit process $\mathbf{y}\to\Gamma_c^+$ in Eq. (34) leads to a degenerate boundary integral equation formulation [7]

$$\frac{1}{2}[u_k(\mathbf{y}\in\Gamma_c^+,t)+u_k(\mathbf{y}\in\Gamma_c^-,t)]$$
$$=u_k^{\mathrm{in}}(\mathbf{y},t)-\text{p.v.}\int_{\Gamma_c^+}h_{ik}(\mathbf{x},\mathbf{y};t)*\Delta u_i(\mathbf{x},t)\mathrm{d}s_x, \tag{37}$$
$$\mathbf{y}\in\Gamma_c^+,$$

where p.v. stands for the Cauchy principal value integral. For a smooth Γ_c^+ and a continuous crack-face loading, a natural way to circumvent this difficulty is the use of the traction BIE formulation. For this purpose, we substitute Eq. (34) into Hooke's law (2) to obtain the following integral representation for the traction components

$$t_j(\mathbf{y},t)=t_j^{\mathrm{in}}(\mathbf{y},t)-\int_{\Gamma_c^+}w_{ij}(\mathbf{x},\mathbf{y};t)*\Delta u_i(\mathbf{x},t)\mathrm{d}s_x,\quad \mathbf{y}\notin\Gamma_c^+, \tag{38}$$

where $w_{ij}(\mathbf{x},\mathbf{y};t)$ is the higher-order traction fundamental solution which is defined by Eq. (23).

Taking the limit process $\mathbf{y}\to\Gamma_c^+$ and invoking the traction boundary conditions (7), time-domain traction BIEs are obtained as

$$\text{p.f.}\int_{\Gamma_c^+}w_{ij}(\mathbf{x},\mathbf{y};t)*\Delta u_i(\mathbf{x},t)\mathrm{d}s_x=t_j^{\mathrm{in}}(\mathbf{y},t),\quad \mathbf{y}\in\Gamma_c^+ \tag{39}$$

where p.f. denotes the Hadamard finite-part integral.

Finally, substitution of Eq. (27) into Eq. (39) leads to

$$\text{p.f.}\int_{\Gamma_c^+}w_{ij}^{\mathrm{s}}(\mathbf{x},\mathbf{y})\Delta u_i(\mathbf{x},t)\mathrm{d}s_x+\int_{\Gamma_c^+}w_{ij}^{\mathrm{d}}(\mathbf{x},\mathbf{y};t)*\Delta\ddot{u}_i(\mathbf{x},t)\mathrm{d}s_x$$
$$=t_j^{\mathrm{in}}(\mathbf{y},t),\quad \mathbf{y}\in\Gamma_c^+. \tag{40}$$

The first term in the time-domain traction BIEs (40) has a hypersingularity and it should be regarded as the Hadamard finite-part integral. In contrast, the second integral in Eq. (40) is regular. To deal with the hypersingular integrals, several analytical and numerical techniques can be found in literature [6,22,31]. In the present paper, a spatial Galerkin-method is applied to regularize the hypersingular BIEs to weakly singular ones. In comparison to other proposed regularization or integration techniques in literature, the Galerkin-method as presented in the next section has the advantage that it regularizes the hypersingular BIEs in a very natural way and does not need any complicated mathematical manipulations.

5. Numerical implementation

To solve the hypersingular time-domain traction BIEs (40) numerically, a time-stepping scheme is developed. The scheme uses the collocation method for the temporal approximation and the Galerkin-method for the spatial discretization of the time-domain traction BIEs. The unknown CODs $\Delta u_i(\mathbf{x},t)$ are approximated by the following interpolation functions

$$\Delta u_i(\mathbf{x},t)=\sum_{q=1}^{Q}\sum_{n=1}^{N}\phi_u^n(\mathbf{x})\varphi_u^q(t)(\Delta u_i)^{nq}, \tag{41}$$

where n denotes the nth node, q represents the qth time-step, $\phi_u^n(\mathbf{x})$ is the spatial shape function (also known as trial or approximating function), and $\varphi_u^q(t)$ is the temporal shape function, respectively. Multiplying both sides of Eq. (40) by the weight-function or test function $\psi_u^m(\mathbf{y})$ and integrating them with respect to s_y we obtain

$$\int_{\Gamma_c^+}\psi_u^m(\mathbf{y})\mathrm{d}s_y\int_{\Gamma_c^+}w_{ij}^{\mathrm{s}}(\mathbf{x},\mathbf{y})\Delta u_i(\mathbf{x},t)\mathrm{d}s_x$$
$$+\int_{\Gamma_c^+}\psi_u^m(\mathbf{y})\mathrm{d}s_y\int_{\Gamma_c^+}w_{ij}^{\mathrm{d}}(\mathbf{x},\mathbf{y};t)*\Delta\ddot{u}_i(\mathbf{x},t)\mathrm{d}s_x$$
$$=\int_{\Gamma_c^+}\psi_u^m(\mathbf{y})t_j^{\mathrm{in}}(\mathbf{y},t)\mathrm{d}s_y,\qquad \mathbf{y}\in\Gamma_c^+. \tag{42}$$

Substitution of the explicit form of the higher-order static traction fundamental solution (30) into Eq. (42) yields

$$\int_{\Gamma_c^+}\psi_u^m(\mathbf{y})\mathrm{d}s_y\int_{\Gamma_c^+}\frac{1}{\pi}\frac{\partial}{\partial s_x}\frac{\partial}{\partial s_y}\mathrm{Im}\sum_{l=1}^{L}B_{ij}^l(\eta_l)\log[\mathbf{d}_l\cdot(\mathbf{x}-\mathbf{y})]$$
$$\Delta u_i(\mathbf{x},t)\mathrm{d}s_x+\int_{\Gamma_c^+}\psi_u^m(\mathbf{y})\mathrm{d}s_y\int_{\Gamma_c^+}w_{ij}^{\mathrm{d}}(\mathbf{x},\mathbf{y};t)*\Delta\ddot{u}_i(\mathbf{x},t)\mathrm{d}s_x$$
$$=\int_{\Gamma_c^+}\psi_u^m(\mathbf{y})t_j^{\mathrm{in}}(\mathbf{y},t)\mathrm{d}s_y,\quad \mathbf{y}\in\Gamma_c^+. \tag{43}$$

Using the technique of partial integration in conjunction with $\psi_u^m=0$ and $\Delta u_i=0$ at the crack-tips, we can transfer the spatial derivatives of the higher-order static traction fundamental solution to the weight-function and the CODs. This results in

$$\int_{\Gamma_c^+}\frac{\partial\psi_u^m(\mathbf{y})}{\partial s_y}\mathrm{d}s_y\int_{\Gamma_c^+}\frac{1}{\pi}\mathrm{Im}\sum_{l=1}^{L}B_{ij}^l(\eta_l)\log[\mathbf{d}_l(\mathbf{x}-\mathbf{y})]\frac{\partial\,\Delta u_i(\mathbf{x},t)}{\partial s_x}\mathrm{d}s_x$$
$$+\int_{\Gamma_c^+}\psi_u^m(\mathbf{y})\mathrm{d}s_y\int_{\Gamma_c^+}w_{ij}^{\mathrm{d}}(\mathbf{x},\mathbf{y};t)*\Delta\ddot{u}_i(\mathbf{x},t)\mathrm{d}s_x$$
$$=\int_{\Gamma_c^+}\psi_u^m(\mathbf{y})t_j^{\mathrm{in}}(\mathbf{y},t)\mathrm{d}s_y,\qquad \mathbf{y}\in\Gamma_c^+. \tag{44}$$

It should be remarked here that the Galerkin-BIEs (44) represent a regularized version of the hypersingular boundary

integral equations (40), and they have only a weak singularity except at the crack-tips, where an additional singularity arises in the spatial derivatives of the CODs.

The crack-face is discretized into straight elements while the time is divided into N constant time-steps, i.e.

$$\Gamma_c^+ = \int_{n=1}^{N} \Gamma_n, \qquad t = Q\,\Delta t, \tag{45}$$

the BIEs (44) can be converted into a system of linear algebraic equations as follows

$$\int_{n=1}^{N} \left(W_{ij}^{s;m,n}(\Delta u_i)^{nQ} + \int_{q=1}^{Q} W_{ij}^{d;m,n,Q-q+1}(\Delta u_i)^{nq} \right) = \int_{n=1}^{N} D^{mn} t_j^{in,nQ}, \tag{46}$$

where the system matrices $W_{ij}^{s;m,n}$, $W_{ij}^{d;m,n,q}$ and D^{mn} are given by

$$W_{ij}^{s;m,n} = \frac{1}{\pi} \int_{\Gamma_m} \frac{\partial \psi_u^m(\mathbf{y})}{\partial s_y} \mathrm{d}s_y \int_{\Gamma_n} \frac{\partial \phi_u^n(\mathbf{x})}{\partial s_x} \mathrm{Im} \sum_{l=1}^{L} \{B_{ij}^l(\eta_l) \log[\mathbf{d}_l \cdot (\mathbf{x}-\mathbf{y})]\} \mathrm{d}s_x, \tag{47}$$

$$W_{ij}^{d;m,n,Q-q+1} = \int_{\Gamma_m} \psi_u^m(\mathbf{y}) \mathrm{d}s_y \int_{\Gamma_n} w_{ij}^d(\mathbf{x},\mathbf{y};Q\,\Delta t) * \ddot{\phi}_u^q(Q\,\Delta t) \phi_u^n(\mathbf{x}) \mathrm{d}s_x, \tag{48}$$

$$D^{mn} = \int_{\Gamma_m} \psi_u^m(\mathbf{y}) \phi_t^n(\mathbf{y}) \mathrm{d}s_y, \tag{49}$$

where $\phi_t^n(\mathbf{y})$ is the spatial shape function for the traction components.

In this analysis, a linear temporal shape function as shown in Fig. 2 is adopted, which can be represented by

$$\begin{aligned} \varphi_u^q(t) = \frac{1}{\Delta t} \{ & [t-(q-1)\Delta t] H[t-(q-1)\Delta t] \\ & -2(t-q\Delta t) H(t-q\,\Delta t) + [t-(q+1)\Delta t] \\ & H[t-(q+1)\Delta t] \}, \end{aligned} \tag{50}$$

where $H(\cdot)$ is the Heaviside step function. The time derivatives of the temporal shape function $\ddot{\phi}_u^q(t)$ is then given by

$$\ddot{\varphi}_u^q(t) = \frac{1}{\Delta t} \{ \delta[t-(q-1)\Delta t] - 2\delta(t-q\,\Delta t) + \delta[t-(q+1)\Delta t] \}. \tag{51}$$

By using Eq. (51) and the sifting property of the Dirac-delta function, the time convolution in Eq. (48) can be evaluated analytically as

$$\begin{aligned} & w_{ij}^d(\mathbf{x},\mathbf{y};Q\,\Delta t) * \ddot{\varphi}_u^q(Q\,\Delta t) \\ & \quad = \frac{1}{\Delta t} \{ w_{ij}^d[\mathbf{x},\mathbf{y};(Q-(q-1))\Delta t)] \\ & \qquad -2w_{ij}^d[\mathbf{x},\mathbf{y};(Q-q)\Delta t] + w_{ij}^d[\mathbf{x},\mathbf{y};(Q-(q+1))\Delta t] \}. \end{aligned} \tag{52}$$

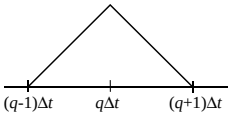

Fig. 2. Temporal shape function $\varphi_u^q(t)$.

As trial or approximating functions, two different spatial shape functions have been adopted, see Fig. 3. For elements away from the crack-tips, we use standard linear shape functions

$$\phi_u^1(\xi) = 1 - \frac{1}{L}\xi, \qquad \phi_u^2(\xi) = \frac{1}{L}\xi, \tag{53}$$

where ξ is the local coordinate with the origin at the beginning of node 1 of the element, and L is the length of the element. At the crack-tips, 'crack-tip elements' defined by

$$\left.\begin{aligned} \phi_u^1(\xi) &= 0 \\ \phi_u^2(\xi) &= \frac{1}{\sqrt{L}}\sqrt{\xi} \end{aligned}\right\} \text{at left crack-tip}, \tag{54}$$

$$\left.\begin{aligned} \phi_u^1(\xi) &= \frac{1}{\sqrt{L}}\sqrt{L-\xi} \\ \phi_u^2(\xi) &= 0 \end{aligned}\right\} \text{at right crack-tip} \tag{55}$$

have been used to adequately describe the local square-root behavior of the CODs near the crack-tips. Thus, the shape function $\phi_u^n(\mathbf{x})$ can be expressed as a function of the local element shape functions $\phi_u^i(\xi)$ as shown in Fig. 3. The shape function for the traction components ϕ_t^n is taken as a linear function. For simplicity, the weight-function is also taken as a linear function. Note that $\psi_u^m(\xi) \neq \phi_u^m(\xi)$ for crack-tip elements.

For the spatial integrations arising in the system matrices, the following cases should be considered:

- *Case 1: Static system matrix, standard elements.* In this case, the arising spatial integral

$$\int_0^{h_m} c\,\mathrm{d}\zeta \int_0^{h_n} a \log(e + f\xi + g\zeta)\mathrm{d}\xi \tag{56}$$

can be integrated analytically and the result is given in Appendix A.

- *Case 2: Static system matrix, crack-tip elements.* In this case, the resulting spatial integral

$$\int_0^{h_m} c\,\mathrm{d}\zeta \int_0^{h_n} \frac{a}{2} \frac{1}{\sqrt{\xi}} \log(e + f\xi + g\zeta)\mathrm{d}\xi \tag{57}$$

can be integrated analytically with respect to ζ, see Appendix A. Then, the integration with respect to ξ is done by using the Gauss–Jacobi quadrature formula to take the $1/\sqrt{\xi}$-singularity of the integrand into account.

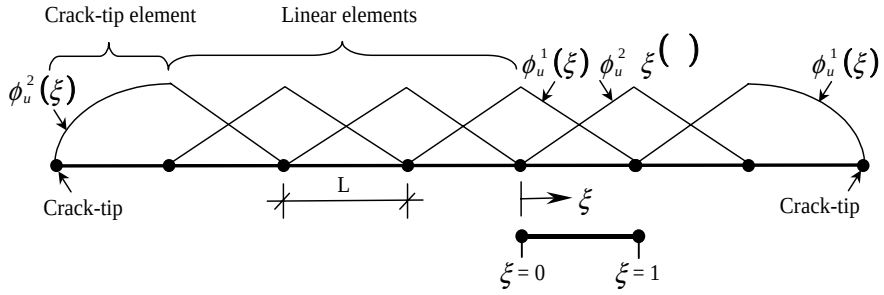

Fig. 3. Spatial shape functions: linear elements away from crack-tips, and 'crack-tip elements' near crack-tips.

- *Case 3: Dynamic system matrix, standard elements.* In this case, the following spatial integral

$$\int_0^{h_m}(c\zeta+d)\mathrm{d}\zeta\int_0^{h_n}(a\xi+b)\frac{1}{e+f\xi+g\zeta}\mathrm{d}\xi \tag{58}$$

can be integrated analytically and the result is given in Appendix B. The remaining integral in the dynamic fundamental solution over the unit circle can be done numerically by using standard Gaussian quadrature formula.

- *Case 4: Dynamic system matrix, crack-tip elements.* The spatial integral to be computed in this case has the following form

$$\int_0^{h_m}(c\zeta+d)\mathrm{d}\zeta\int_0^{h_n}(a\sqrt{\xi}+b)\frac{1}{e+f\xi+g\zeta}\mathrm{d}\xi. \tag{59}$$

Here, the integration with respect to ζ can be performed analytically, see Appendix B. Then, the integrations with respect to ξ and over the unit circle in the dynamic fundamental solution are carried out numerically by using standard Gaussian quadrature formula.

After the system matrices have been computed, the discrete CODs can be computed numerically by using the explicit time-stepping scheme (46) step by step.

6. Dynamic stress intensity factors

In the vicinity of a crack-tip in an anisotropic and linearly elastic solid, the asymptotic displacement field is given by [21]

$$\begin{aligned}u_1=\sqrt{\frac{2r}{\pi}}\Bigg\{&K_{\mathrm{I}}\,\mathrm{Re}\left[\frac{1}{\mu_1-\mu_2}(\mu_1p_2\sqrt{\cos\theta+\mu_2\sin\theta}\right.\\&\left.-\mu_2p_1\sqrt{\cos\theta+\mu_1\sin\theta})\right]\\&+K_{\mathrm{II}}\,\mathrm{Re}\left[\frac{1}{\mu_1-\mu_2}(p_2\sqrt{\cos\theta+\mu_2\sin\theta}\right.\\&\left.-p_1\sqrt{\cos\theta+\mu_1\sin\theta})\right]\Bigg\},\end{aligned} \tag{60}$$

$$\begin{aligned}u_2=\sqrt{\frac{2r}{\pi}}\Bigg\{&K_{\mathrm{I}}\,\mathrm{Re}\left[\frac{1}{\mu_1-\mu_2}(\mu_1q_2\sqrt{\cos\theta+\mu_2\sin\theta}\right.\\&\left.-\mu_2q_1\sqrt{\cos\theta+\mu_1\sin\theta})\right]\\&+K_{\mathrm{II}}\,\mathrm{Re}\left[\frac{1}{\mu_1-\mu_2}(q_2\sqrt{\cos\theta+\mu_2\sin\theta}\right.\\&\left.-q_1\sqrt{\cos\theta+\mu_1\sin\theta})\right]\Bigg\},\end{aligned} \tag{61}$$

$$u_3=K_{\mathrm{III}}\sqrt{\frac{2r}{\pi}}(C_{44}C_{55}-C_{45}^2)^{-1/2}\mathrm{Im}[(\cos\theta+\mu_3\sin\theta)^{1/2}], \tag{62}$$

where r and θ are polar coordinates with the origin at the crack-tip, K_{I}, K_{II} and K_{III} represent the mode-I, mode-II and mode-III stress intensity factors, μ_α are the complex roots of the material characteristic equation

$$b_{11}\mu_\alpha^4-2b_{16}\mu_\alpha^3+(2b_{12}+b_{66})\mu_\alpha^2-2b_{26}\mu_\alpha+b_{22}=0, \tag{63}$$

with b_{ij} $(i,j=1,2,6)$ being the material compliance matrix

$$\begin{aligned}p_\alpha&=b_{11}\mu_\alpha^2+b_{12}-b_{16}\mu_\alpha,\\q_\alpha&=(b_{12}\mu_\alpha^2+b_{22}-b_{26}\mu_\alpha)/\mu_\alpha,\end{aligned} \tag{64}$$

and μ_3 is the complex root of

$$C_{44}\mu_3^2+2C_{45}\mu_3+C_{55}=0, \tag{65}$$

with positive imaginary part. Eqs. (60)–(62) lead to the following relations between the elastodynamic stress intensity factors and the CODs

$$\begin{Bmatrix}K_{\mathrm{I}}(t)\\K_{\mathrm{II}}(t)\end{Bmatrix}=\frac{\sqrt{2\pi}}{4\Delta}\begin{bmatrix}H_{11}&H_{12}\\H_{21}&H_{22}\end{bmatrix}\lim_{r\to0}\frac{1}{\sqrt{r}}\begin{Bmatrix}\Delta u_1(r,t)\\\Delta u_2(r,t)\end{Bmatrix}, \tag{66}$$

$$K_{\mathrm{III}}(t)=\frac{\sqrt{2\pi}}{4}\sqrt{C_{44}C_{55}-C_{45}^2}\lim_{r\to0}\frac{1}{\sqrt{r}}\Delta u_3(r,t), \tag{67}$$

where

$$\begin{bmatrix} H_{11} & H_{12} \\ H_{21} & H_{22} \end{bmatrix} = \begin{bmatrix} \mathrm{Im}\left(\frac{q_1-q_2}{\mu_1-\mu_2}\right) & \mathrm{Im}\left(\frac{p_2-p_1}{\mu_1-\mu_2}\right) \\ \mathrm{Im}\left(\frac{\mu_1 q_2-\mu_2 q_1}{\mu_1-\mu_2}\right) & \mathrm{Im}\left(\frac{\mu_2 p_1-\mu_1 p_2}{\mu_1-\mu_2}\right) \end{bmatrix}, \tag{68}$$

$$\Delta = H_{11}H_{22}-H_{12}H_{21}. \tag{69}$$

The mode-I and the mode-II elastodynamic stress intensity factors can be calculated numerically by using Eq. (66) and the mode-III can be determined using Eq. (67), after the CODs have been computed numerically by using the time-stepping scheme (46).

7. Numerical examples

To verify the accuracy of the present time-domain traction BEM, let us first consider a straight crack of length $2a$ in an infinite, linearly elastic and isotropic solid as shown in Fig. 4. The cracked solid is subjected either to an incident plane longitudinal wave (L-wave) loading of the form

$$u_\alpha^{\mathrm{in}}(\mathbf{x}) = U_{\mathrm{L}} D_\alpha [c_{\mathrm{L}} t-(x_1+a)\sin\theta - x_2\cos\theta] H[c_{\mathrm{L}} t - (x_1+a)\sin\theta - x_2\cos\theta], \tag{70}$$

or to an incident plane transverse wave (T-wave) loading of the form

$$u_\alpha^{\mathrm{in}}(\mathbf{x}) = U_{\mathrm{T}} B_\alpha [c_{\mathrm{T}} t-(x_1+a)\sin\theta - x_2\cos\theta] H[c_{\mathrm{T}} t - (x_1+a)\sin\theta - x_2\cos\theta], \tag{71}$$

where θ is the incidence angle, $\mathbf{D}=(\sin\theta,\ \cos\theta)^{\mathrm{T}}$ and $\mathbf{B}=(-\cos\theta,\ \sin\theta)^{\mathrm{T}}$ are the vibration direction vectors for incident L- and T-waves in the isotropic solids, U_{L} and U_{T} are the displacement amplitudes of the incident L- and T-waves, $H[\cdot]$ is the Heaviside function, and c_{L} and c_{T} are the longitudinal and transverse wave velocities, respectively. Plane strain condition is assumed. For anisotropic solids, the in-plane and out-of-plane mechanical motions are generally coupled. The present method can handle the in-plane and out-of-plane coupling. To test the accuracy of the present method for anti-plane analysis, let us consider an incident plane TH-wave (horizontally polarized shear wave) of the form

$$u_3^{\mathrm{in}}(\mathbf{x}) = U_3[c_{\mathrm{T}} t-(x_1+a)\sin\theta - x_2\cos\theta] H[c_{\mathrm{T}} t - (x_1+a)\sin\theta - x_2\cos\theta], \tag{72}$$

where c_{T} here is the phase velocity of the TH-wave and U_3 is the amplitude factor. For convenience, the dynamic stress intensity factors are normalized by the corresponding values,

$$\bar{K}_{\mathrm{I}}^{\pm}(t) = K_{\mathrm{I}}^{\pm}(t)/K_{\mathrm{I}}^{\mathrm{st}}, \qquad \bar{K}_{\mathrm{II}}^{\pm}(t) = K_{\mathrm{II}}^{\pm}(t)/K_{\mathrm{II}}^{\mathrm{st}}, \qquad \bar{K}_{\mathrm{III}}^{\pm}(t) = K_{\mathrm{III}}^{\pm}(t)/K_{\mathrm{III}}^{\mathrm{st}} \tag{73}$$

where the static stress intensity factors are given by

$$K_{\mathrm{I}}^{\mathrm{st}} = \sigma_{22}\sqrt{\pi a}, \qquad K_{\mathrm{II}}^{\mathrm{st}} = \sigma_{12}\sqrt{\pi a}, \qquad K_{\mathrm{III}}^{\mathrm{st}} = \sigma_{32}\sqrt{\pi a}, \tag{74}$$

with $\sigma_{i\alpha}$ being the stress amplitudes of the remote a remote static stress loading at infinity. In Eq. (73), '+' denotes the right crack-tip $x_1=+a$, while '−' represents the left crack-tip at $x_1=-a$.

For comparisons, an isotropic material is first selected with Poisson's ratio of $\nu=0.25$. The crack is divided into 20 elements of equal size. The time-step is taken as $c_{\mathrm{T}}\,\Delta t/a=0.1$ with c_{T} being the transverse wave speed. The selected time-step corresponds to the time required by the transverse wave to pass one element-length. For L-waves with $\theta=0$ and 30°, the normalized mode-I dynamic stress intensity factors $\bar{K}_{\mathrm{I}}$ versus the dimensionless time $c_{\mathrm{L}}t/a$ are presented in Figs. 5 and 6. Results of the normalized mode-II dynamic stress intensity factors $\bar{K}_{\mathrm{II}}$ for the 30° L-wave is presented in Fig. 7. In these figures, our numerical results are compared to the analytical results of Thau and Lu [27] and the numerical ones obtained by Zhang and Savaidis via a hypersingular time-domain BEM [32]. The comparison shows good agreement between our numerical results, the analytical results of Thau and Lu [27],

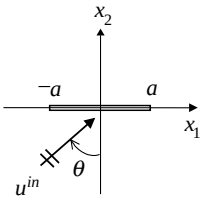

Fig. 4. A finite crack of length $2a$ subjected to an incident wave loading.

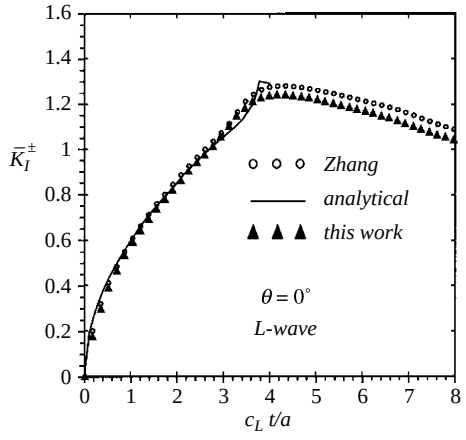

Fig. 5. Normalized dynamic stress intensity factors ($\bar{K}_{\mathrm{I}}^{\pm}$) in an isotropic solid subjected to a normal incidence of a plane L-wave.

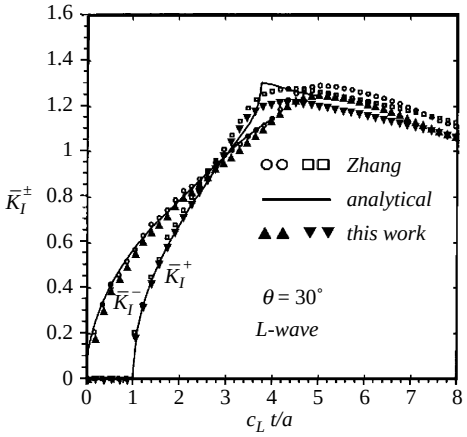

Fig. 6. Normalized dynamic stress intensity factors ($\bar{K}_{\mathrm{I}}^{\pm}$) in an isotropic solid subjected to a 30° incidence of a plane L-wave.

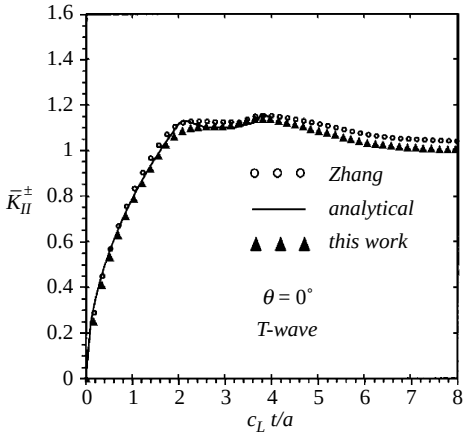

Fig. 8. Normalized dynamic stress intensity factors ($\bar{K}_{\mathrm{II}}^{\pm}$) in an isotropic solid subjected to a normal incidence of a plane T-wave.

and the numerical ones of Zhang and Savaidis [32]. For a normal incidence of a plane transverse wave (T-wave) with $\theta = 0°$, the normalized mode-II dynamic stress intensity factor is shown in Fig. 8. A comparison with the analytical and other numerical results shows again a good agreement. As in the case of an incident plane L-wave, the normalized dynamic stress intensity factor increases first with increasing time and after reaching its maximum value it decreases slowly in magnitude and approaches the corresponding static value. Also, dynamic overshoots are induced due the interaction of the crack with the incident waves. Figs. 9 and 10 show the normalized mode-I and mode-II dynamic stress intensity factors for a 30° incidence of T-wave, respectively.

An isotropic solid is also considered for the anti-plane analysis and then compared to the solution of Thau and Lu [26] and the anti-plane analysis of Zhang [33]. Numerical calculations are carried out for a normal incidence of a planar TH-wave. The time step is now taken as $c_{\mathrm{T}}\,\Delta t/a = 0.05$. The crack is divided into 40 elements of equal size. A comparison of the present results with the analytical results and with that of Zhang's anti-plane analysis as shown in Fig. 11 confirms the accuracy of the present method.

It should be noted that for the analytical methods shown here, sharp kinks at the peak of the dynamic SIFs are produced. These kinks are due to the arrival of the wavefront produced by the diffraction from the opposite crack. The stress intensity factors are functions of the crack-tip CODs. Since element-wise approximation is used for the CODs, these sharp kinks are difficult to reproduce. The present numerical method shows a limitation in expressing the sudden change in the crack opening displacement.

In the next example, we consider a finite straight crack of length $2a$ in an infinite, transversely isotropic and linearly elastic solid subjected to the same impact incident wave loading as described by Eq. (70), where c_{L} is replaced by c'_L and denotes the quasi-longitudinal wave speed. The vibration direction in this case is, however, different to that in isotropic solids, i.e. $\mathbf{D} \neq (\sin\theta, \cos\theta)^{\mathrm{T}}$ in anisotropic solids. The elastic constants (in GPa) used are

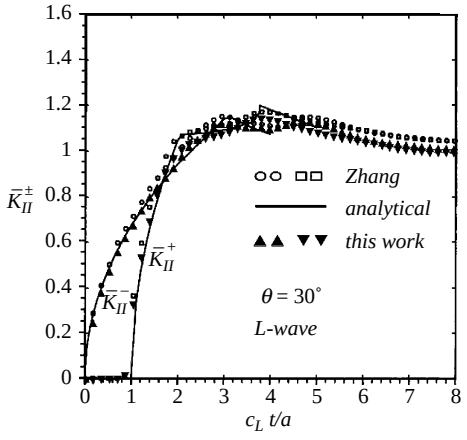

Fig. 7. Normalized dynamic stress intensity factors ($\bar{K}_{\mathrm{II}}^{\pm}$) in an isotropic solid subjected to a 30° incidence of a plane L-wave.

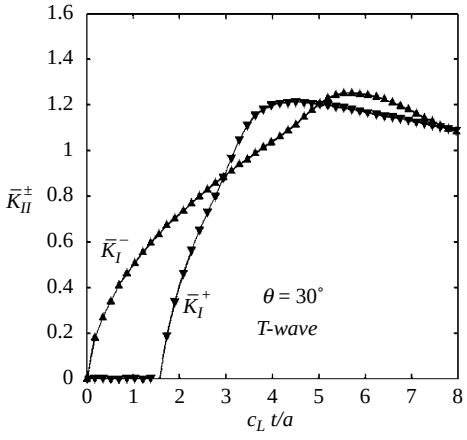

Fig. 9. Normalized dynamic stress intensity factors ($\bar{K}_{\mathrm{I}}^{\pm}$) in an isotropic solid subjected to a 30° incidence of a plane T-wave.

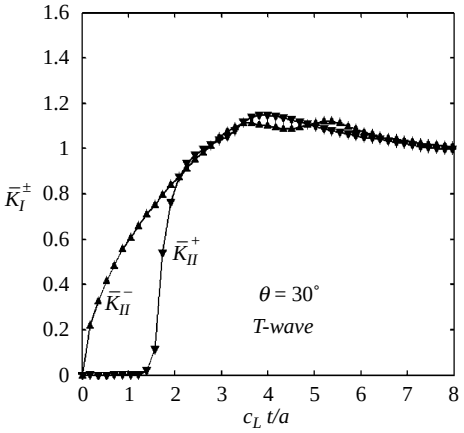

Fig. 10. Normalized dynamic stress intensity factors ($\bar{K}_{\mathrm{II}}^{\pm}$) in an isotropic solid subjected to a 30° incidence of a plane T-wave.

$$\begin{bmatrix} C_{11} & C_{12} & C_{13} & C_{14} & C_{15} & C_{16} \\ & C_{22} & C_{23} & C_{24} & C_{25} & C_{26} \\ & & C_{33} & C_{34} & C_{35} & C_{36} \\ & & & C_{44} & C_{45} & C_{46} \\ & \text{sym} & & & C_{55} & C_{56} \\ & & & & & C_{66} \end{bmatrix}$$

$$= \begin{bmatrix} 160.7 & 6.44 & 146.56 & 0 & 0 & 0 \\ & 13.92 & 6.44 & 0 & 0 & 0 \\ & & 160.70 & 0 & 0 & 0 \\ & & & 3.5 & 0 & 0 \\ & \text{sym} & & & 7.07 & 0 \\ & & & & & 3.5 \end{bmatrix}$$

These elastic constants correspond to a graphite-epoxy composite [17]. The x_1-axis is taken as the axis of symmetry for the transversely isotropic solid. The time-step is selected as $\sqrt{C_{66}/\rho}\,\Delta t/a = 0.1$ and 20 elements are used.

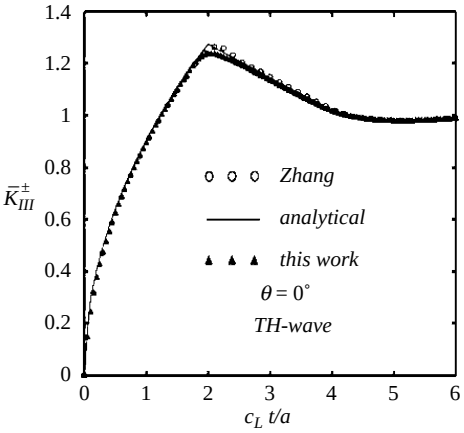

Fig. 11. Normalized dynamic stress intensity factors ($\bar{K}_{\mathrm{III}}^{+}$) in an isotropic solid subjected to a normal incidence of a plane TH-wave.

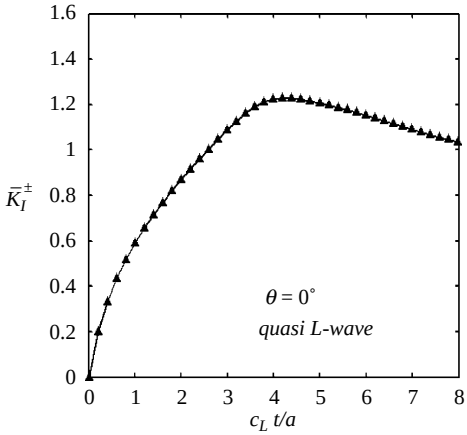

Fig. 12. Normalized dynamic stress intensity factors ($\bar{K}_{\mathrm{I}}^{\pm}$) in a transversely isotropic solid subjected to a normal incidence of a quasi-L-wave.

In Figs. 12 and 13, the normalized mode-I dynamic stress intensity factors are given, for an incident quasi-longitudinal wave with the incidence angles $\theta = 0$ and 30°, respectively. Fig. 14 shows the normalized mode-II dynamic stress intensity factor for the 30° oblique incidence of the quasi-L-wave. Similar to the isotropic solids, the dynamic stress intensity factors are normalized by the corresponding static stress intensity factor for anisotropic solids and the time is normalized to $c'_{\mathrm{L}}t/a$. A comparison of Figs. 12 and 13 with Figs. 5 and 6 show that the normalized dynamic stress intensity factors for the considered transversely isotropic solid are very similar to that for the isotropic solid. The slight difference in the $\bar{K}_{\mathrm{I}}^{+}(t)$-curve for $\theta = 30°$ in the small time range lies in the fact that the wave velocity in the x_1-direction is much larger for the transversely isotropic solid than that for the isotropic one. This implies that the quasi-longitudinal wave in the transversely isotropic solid arrives the right crack-tip much earlier than that in the isotropic one.

Finally, we consider a finite crack in a trigonal solid. For this purpose, the quartz is chosen. The elastic constants in GPa are given by

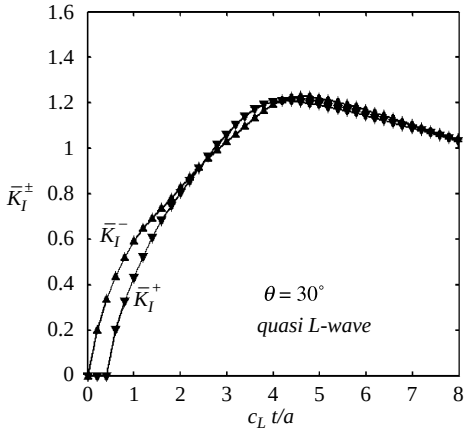

Fig. 13. Normalized dynamic stress intensity factors ($\bar{K}_{\mathrm{I}}^{\pm}$) in a transversely isotropic solid subjected to a 30° incidence of a quasi-L-wave.

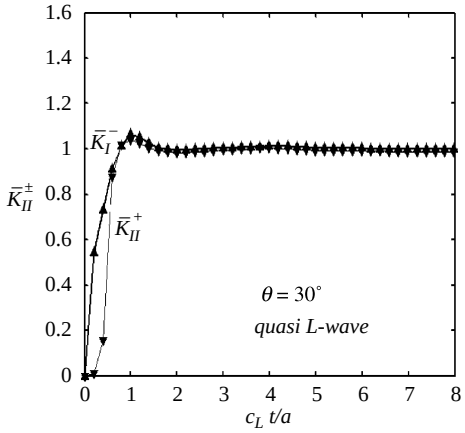

Fig. 14. Normalized dynamic stress intensity factors ($\bar{K}_{\mathrm{II}}^{\pm}$) in a transversely isotropic solid subjected to a 30° incidence of a quasi-L-wave.

$$\begin{bmatrix} C_{11} & C_{12} & C_{13} & C_{14} & C_{15} & C_{16} \\ & C_{22} & C_{23} & C_{24} & C_{25} & C_{26} \\ & & C_{33} & C_{34} & C_{35} & C_{36} \\ & & & C_{44} & C_{45} & C_{46} \\ & \text{sym} & & & C_{55} & C_{56} \\ & & & & & C_{66} \end{bmatrix}$$

$$= \begin{bmatrix} 8.674 & 0.699 & 0.699 & -1.791 & 0 & 0 \\ & 8.674 & 0.699 & 1.791 & 0 & 0 \\ & & 10.72 & 0 & 0 & 0 \\ & & & 5.794 & 0 & 0 \\ & \text{sym} & & & 5.794 & -1.791 \\ & & & & & 3.988 \end{bmatrix}$$

A time-step of $\sqrt{C_{66}/\rho}\,\Delta t/a = 0.05$ and 40 elements are now used for the numerical calculations of the quartz. In Figs. 15 and 16, the normalized dynamic stress intensity mode-I factor is presented for a normal incidence of quasi-L-wave and an oblique incidence of a plane L-wave with $\theta = 30°$, respectively,

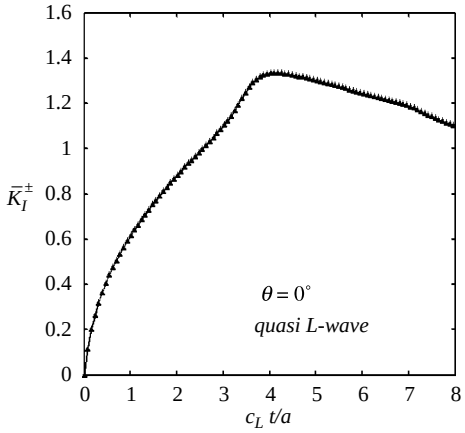

Fig. 15. Normalized dynamic stress intensity factors ($\bar{K}_{\mathrm{I}}^{\pm}$) for a quartz subjected to a normal incidence of a quasi-L-wave with infinite duration.

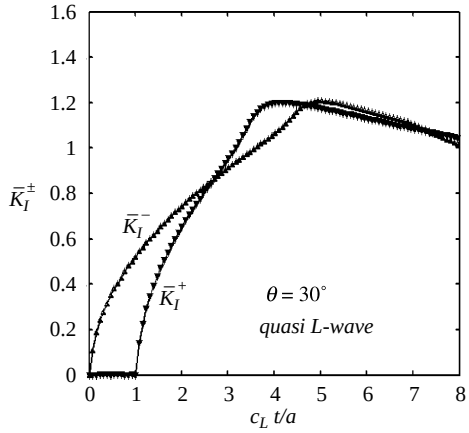

Fig. 16. Normalized dynamic stress intensity factors ($\bar{K}_{\mathrm{I}}^{\pm}$) for a quartz subjected to a 30° incidence of a quasi-L-wave with infinite duration.

while Fig. 17 shows the $\bar{K}_{\mathrm{II}}^{\pm}$ for the 30° oblique incidence of the quasi-L-wave. An infinite duration of the wave pulse is used, which is described by Eq. (70) with $\mathbf{D} \neq (\sin\theta, \cos\theta)^{\mathrm{T}}$. The corresponding numerical results for the triangular pulse shape are given in Figs. 18–20. The considered triangular pulse shape is depicted in Fig. 21, which can be described by

$$u_i^{\mathrm{in}}(\mathbf{x}) = \frac{u_0}{\delta} D_i[pH(p) - 2(p-\delta)H(p-\delta) - (p-2\delta)H(p-2\delta)], \tag{75}$$

where u_0 is the amplitude and 2δ is the base of the triangular pulse, and

$$p = t - \frac{(x_2 + a)\sin\theta}{c'_L} - \frac{x_1 \cos\theta}{c'_L}, \qquad \delta = \frac{0.25a}{c'_L}, \tag{76}$$

with c'_{L} being the velocity of the incident quasi-L-wave. Figs. 18–20 show that a triangular pulse shape may give rise to negative mode-I dynamic stress intensity factors, which means physically that the crack-faces may come into contact in this loading case.

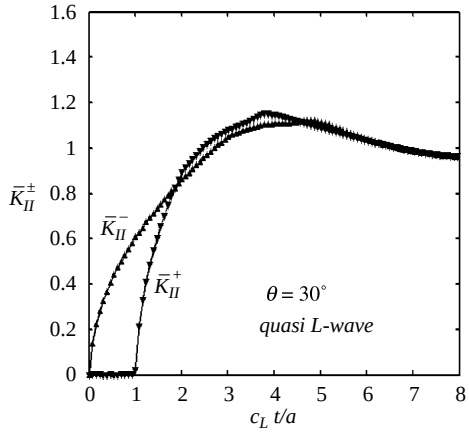

Fig. 17. Normalized dynamic stress intensity factors ($\bar{K}_{\mathrm{II}}^{\pm}$) for a quartz subjected to a 30° incidence of a quasi-L-wave with infinite duration.

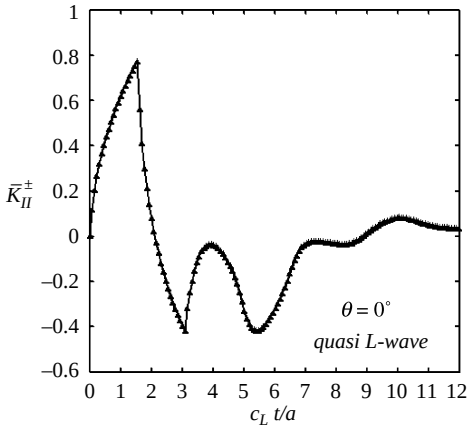

Fig. 18. Normalized dynamic stress intensity factors ($\bar{K}_{\mathrm{I}}^{\pm}$) for a quartz subjected to a normal incidence of a quasi-L-wave with a triangular shaped pulse.

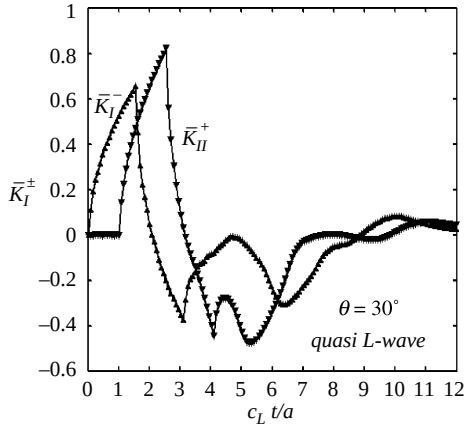

Fig. 19. Normalized dynamic stress intensity factors ($\bar{K}_{\mathrm{I}}^{\pm}$) for a quartz subjected to a 30° incidence of a quasi-L-wave with a triangular shaped pulse.

8. Conclusions

In this paper, a 2D time-domain collocation-Galerkin BEM is presented for transient elastodynamic crack analysis in homogeneous, anisotropic and linear elastic solids. For the temporal approximation, a collocation method is adopted which uses a linear temporal shape function. For the spatial discretization, two different shape functions are applied. For elements away from the crack-tips, linear spatial shape functions are used, while at the crack-tips 'crack-tip elements' are utilized to describe the local 'square-root' behavior of the CODs near the crack-tips. This enables us to compute the dynamic stress intensity factors very accurately. The time convolution can be computed analytically. In the case of linear elements, the spatial integrations can also be calculated analytically. For crack-tip elements, the spatial integrations are integrated analytically and numerically. The integral over the unit circle in the dynamic fundamental solutions has to be computed numerically. The system matrices are symmetric and no special integration techniques are required, since the arising hypersingular integrals are first regularized to weakly singular integrals by applying the Galerkin-method. Numerical results for the dynamic stress intensity factors are presented and discussed to demonstrate the accuracy and the efficiency of the present time-domain BEM.

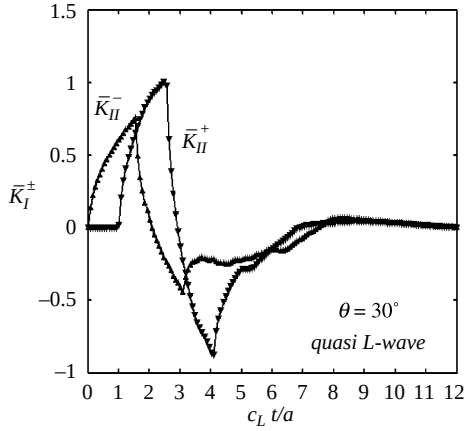

Fig. 20. Normalized dynamic stress intensity factors ($\bar{K}_{\mathrm{II}}^{\pm}$) for a quartz subjected to a 30° incidence of a quasi-L-wave with a triangular shaped pulse.

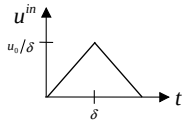

Fig. 21. Triangular pulse.

Acknowledgements

The work of Ch. Zhang is supported by the German Research Foundation (DFG) under the project number ZH 15/5-1, which is gratefully acknowledged. A. Tan would also like to acknowledge the support from the University of the Philippines Diliman, where he is currently under study leave.

Appendix A. Computation of the static system matrix

For the integration of the static system matrix, it is convenient to introduce a local coordinate ζ for the element Γ_m and another local coordinate ξ for the element Γ_n, see Fig. A1. Then, Eq. (47) can be written as

$$W_{ij}^{s;m,n} = \frac{1}{\pi}\int_0^{h_m} \frac{\partial \psi_u^m(\zeta)}{\partial \zeta}\mathrm{d}\zeta \int_0^{h_n} \frac{\partial \phi_u^n(\xi)}{\partial \xi}\mathrm{Im} \int_{l=1}^{L} \{B_{ij}^l(\eta_l)\log[\mathbf{d}_l\cdot(\mathbf{x}^{n-1}-\mathbf{y}^{m-1}) + \mathbf{d}_l\cdot\mathbf{s}^n\xi - \mathbf{d}_l\cdot\mathbf{s}^m\zeta]\}\mathrm{d}\xi, \tag{A1}$$

where h_m and h_n denote the lengths of the mth element and the nth element, while $\mathbf{s}^m$ and $\mathbf{s}^n$ represent the unit vectors along the straight elements Γ_m and Γ_n (see Fig. A1).

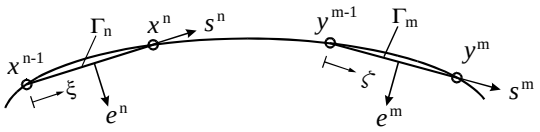

Fig. A1. Discretization of the crack-face.

A.1. Standard elements

With the following weight- and approximating functions and their derivatives

$$\psi_u^m(\zeta) = c\zeta + d, \Rightarrow \frac{\partial \psi_u^m(\zeta)}{\partial \zeta} = c,$$
$$\phi_u^n(\xi) = a\xi + b, \Rightarrow \frac{\partial \phi_u^n(\xi)}{\partial \xi} = a, \tag{A2}$$

as well as the abbreviations

$$e = \mathbf{d}_l \cdot (\mathbf{x}^{n-1} - \mathbf{y}^{m-1}), \qquad f = \mathbf{d}_l \cdot \mathbf{s}^n, \qquad g = -\mathbf{d}_l \cdot \mathbf{s}^m, \tag{A3}$$

we obtain the following analytical result for the integral in Eq. (A1)

$$\begin{aligned}
&\int_0^{h_m} c\,\mathrm{d}\zeta \int_0^{h_n} a\,\log(e + f\xi + g\zeta)\mathrm{d}\xi \\
&= \frac{ace^2\log(e)}{2fg} - \frac{ac(e+gh_m)^2\log(e+gh_m)}{2fg} \\
&\quad - \frac{ac(e+fh_n)^2\log(e+fh_n)}{2fg} \\
&\quad + \frac{ac(e+fh_n+gh_m)^2\log(e+fh_n+gh_m)}{2fg} \\
&\quad - \frac{3ach_mh_n}{2}.
\end{aligned} \tag{A4}$$

It should be noted here that e, f and g in Eq. (A4) are complex constants. Since the complex log-function is multi-valued, the branch-cuts of the log-function must be properly chosen.

A.2. Crack-tip elements

In this case, the weight- and the approximating functions as well as their derivatives are given by

$$\psi_u^m(\zeta) = c\zeta + d, \Rightarrow \frac{\partial \psi_u^m(\zeta)}{\partial \zeta} = c,$$
$$\phi_u^n(\xi) = a\sqrt{\xi} + b, \Rightarrow \frac{\partial \phi_u^n(\xi)}{\partial \xi} = \frac{a}{2}\frac{1}{\sqrt{\xi}}. \tag{A5}$$

The integral in Eq. (A1) can be integrated analytically with respect to ζ

$$\begin{aligned}
&\int_0^{h_m} c\,\mathrm{d}\zeta \int_0^{h_n} \frac{a}{2}\frac{1}{\sqrt{\xi}}\log(e + f\xi + g\zeta)\mathrm{d}\xi \\
&= \int_0^{h_n} \left\{ \frac{1}{2}\frac{ca(e+f\xi+gh_m)\log(e+f\xi+gh_m)}{g\sqrt{\xi}} \right\}\mathrm{d}\xi. \\
&\quad - \frac{1}{2}\frac{ca(e+f\xi)\log(e+f\xi)}{g\sqrt{\xi}} - \frac{cah_m}{2\sqrt{\xi}}
\end{aligned} \tag{A6}$$

The remaining integral in Eq. (A6) can be computed numerically by using the Gauss–Jacobi quadrature formula to take the $1/\sqrt{\xi}$-singularity of the integrand into account.

Appendix B. Computation of the dynamic system matrix

To perform the spatial integration of the dynamic system matrix, we first substitute Eq. (52) into Eq. (48). Then, it is sufficient to consider the following integral

$$\int_{\Gamma_m} \psi_u^m(\mathbf{y})\mathrm{d}s_y \int_{\Gamma_n} \frac{1}{c_l q\,\Delta t + \mathbf{n}\cdot(\mathbf{x}-\mathbf{y})}\phi_u^n(x)\mathrm{d}s_x. \tag{B1}$$

By using the local coordinates ζ and ξ and the abbreviations

$$e = c_l q\,\Delta t + \mathbf{n}\cdot(\mathbf{x}^{n-1} - \mathbf{y}^{m-1}), \qquad f = \mathbf{n}\cdot\mathbf{s}^n,$$
$$g = -\mathbf{n}\cdot\mathbf{s}^m, \tag{B2}$$

Eq. (B1) can be recast into

$$\int_0^{h_m} \psi_u^m(\zeta)\mathrm{d}\zeta \int_0^{h_n} \phi_u^n(\xi)\frac{1}{e + f\xi + g\zeta}\mathrm{d}\xi. \tag{B3}$$

B.1. Standard elements

Substitution of the weight- and the approximating functions (A2) into the integral (B3) results in the following analytical result

$$\begin{aligned}
&\int_0^{h_m} (c\zeta + d)\mathrm{d}\zeta \int_0^{h_n} (a\xi + b)\frac{1}{e + f\xi + g\zeta}\mathrm{d}\xi \\
&= A_1\, e\log(e) - A_2(e+gh_m)\log(e+gh_m) + A_3(e \\
&\quad + fh_n)\log(e+fh_n) - A_4(e+fh_n+gh_m)\log(e \\
&\quad + fh_n + gh_m) + A_5,
\end{aligned} \tag{B4}$$

where

$$A_1 = (-3bcef + ace^2 - 3adeg + 6bdfg)/(6f^2g^2), \tag{B5}$$

$$A_2 = A_1 + (-2acg^2h_m - 3adg^2 + 3bcfg - aceg)h_m/(6f^2g^2), \tag{B6}$$

$$A_3 = -A_1 + (2acf^2h_n + 3adfg + 3bcf^2 - acef)h_n/(6f^2g^2), \tag{B7}$$

$$A_4 = -A_1 - [(2acg^2h_m + 3adg^2 + 3bcfg + aceg)h_m + 2acfgh_mh_n - (2acf^2h_n + 3bcf^2 - 3adfg + acef)h_n]/(6f^2g^2), \tag{B8}$$

$$A_5 = (3adg + 2acgh_m + 2acfh_n + 3bcf + ace)h_mh_n/(6fg). \tag{B9}$$

B.2. Crack-tip elements

Substitution of the weight- and the approximating functions (A5) into the integral (B3) and integration with respect to ζ leads to the result

$$\int_0^{h_m}(c\zeta + d)\mathrm{d}\zeta \int_0^{h_n}(a\sqrt{\xi} + b)\frac{1}{e + f\xi + g\zeta}\mathrm{d}\xi = \int_0^{h_n}\left\{\frac{a\sqrt{\xi}(gd - ce - cf\xi)\log(e + f\xi + gh_m)}{g^2} - \frac{a\sqrt{\xi}(gd - ce - cf\xi)\log(e + f\xi)}{g^2} + \frac{a\sqrt{\xi}ch_m}{g}\right\}\mathrm{d}\xi. \tag{B10}$$

The remaining integral in Eq. (B10) can be computed numerically by using the standard Gaussian quadrature formula.

It should be noted that the integral over the unit circle appearing in the dynamic fundamental solutions cannot be integrated analytically and has to be computed numerically by using the standard Gaussian quadrature formula.

References

[1] Achenbach, Achenbach JD. Wave propagation in elastic solids. Amsterdam/New York: North-Holland; 1973.

[2] Albuquerque EL, Sollero P, Aliabadi MH. The boundary element method applied to time dependent problems. Int J Solids Struct 2002;39:1405–22.

[3] Albuquerque EL, Sollero P, Fedelinsky P. Dual reciprocity boundary element method in Laplace-domain applied to anisotropic dynamic crack problems. Comput Struct 2003;81:1703–13.

[4] Albuquerque EL, Sollero P, Aliabadi MH. Dual boundary element method for anisotropic dynamic fracture mechanics. Int J Numer Meth Eng 2004;59:1187–205.

[5] Aliabadi MH, Rooke DP. Numerical fracture mechanics. Southampton, UK & Boston, USA: Computational Mechanics Publications; 1991.

[6] Chen JT, Hong H-K. Review of dual boundary element methods with emphasis on hypersingular integrals and divergent series. Appl Mech Rev 1999;52:17–33.

[7] Cruse TA, Cruse TA. Boundary element analysis in computational fracture mechanics. Boston, Mass: Kluwer Academic Publishers; 1988.

[8] Denda M, Wang CY, Yong YC. 2-D time-harmonic BEM for solids of general anisotropy with application to eigenvalue problems. J. Sound Vibration 2003;261:247–76.

[9] Denda M, Marante ME. Mixed mode BEM analysis of multiple curvilinear cracks in the general anisotropic solids by the crack tip singular element. Int J Solids Struct 2004;41(5–6):1473–89.

[10] Garcia F, Saez A, Dominguez J. Traction boundary elements for cracks in anisotropic solids. Eng Anal Bound Elem 2004;28:667–76.

[11] Garcia F, Saez A, Dominguez J. Anisotropic and piezoelectric materials fracture analysis by BEM. Comput Struct 2005;83:804–20.

[12] Hirose S, Achenbach JD. Time-domain boundary element analysis of elastic wave interaction with a crack. Int J Numer Meth Eng 1989;28: 629–44.

[13] Hirose S. Dynamic analysis for a crack in anisotropic elastic solid (in Japanese). JASCOME 1999;16:13–17.

[14] Hirose, S., Wang, C.-Y. and Achenbach, J. D.: Boundary element method for elastic wave scattering by a crack in an anisotropic solid. 20th Int. Congress Theoret. Appl. Mech. ICTAM 2000, Chicago, USA, 27 August - 2 September 2000.

[15] Hirose S, Zhang Ch, Wang C-Y. A comparative study on two time-domain BEM/BIEM for transient dynamic crack analysis of anisotropic solids. In: Zhenhan Y, Aliabadi MH, editors. Boundary element techniques. Shanghai, PR China: Tsinghua University Press; 2002. p. 106–12.

[16] Izumi, A. and Hirose, S.: Crack Growth Analysis in Anisotropic Solids. Technical Report. No. 62. Department of Civil Engineering. Tokyo Institute of Technology, Tokyo, Japan, pp. 3-15, 2000.

[17] Musgrave MJ, Musgrave MJP. Crystal acoustics. San Francisco, USA: Holden-Day, Inc.; 1970.

[18] Pan E, Amadei B. Fracture mechanics analysis of cracked 2-D anisotropic media with a new formulation of the boundary element method. Int J Fract 1996;64:161–74.

[19] Pan E. A BEM analysis of fracture mechanics in 2D anisotropic piezoelectric solids. Eng Anal Bound Elem 1999;23:67–76.

[20] Saez A, Dominguez J. BEM analysis of wave scattering in transversely isotropic solids. Int J Numer Meth Eng 1999;44:1283–300.

[21] Sih GC, Paris PC, Irwin GR. On cracks in rectlinearly anisotropic bodies. Int J Fract 1965;1:189–203.

[22] Sladek V, Sladek J. Regularization of hypersingular integrals in BEM formulations using various kinds of continuous elements. Eng Anal Bound Elem 1996;17:5–18.

[23] Snyder MD, Cruse TA. Boundary integral equation analysis of cracked anisotropic plates. Int J Fract 1975;11:315–28.

[24] Sollero P, Aliabadi MH. Fracture mechanics analysis of anisotropic plates by the boundary element method. Int J Fract 1993;64:269–84.

[25] Tan, A., Hirose, S., Zhang, Ch. and Wang, C.-Y.: A 2D time-domain BEM for transient wave scattering analysis by a crack in anisotropic solids. Eng. Anal. with Bound. Elem., 2005;6:610–623.

[26] Thau SA, Lu TH. Diffraction of transient horizontal shear waves by a finite crack and a finite rigid ribbon. Int J Eng Sci 1970;8:857–74.

[27] Thau SA, Lu TH. Transient stress intensity factors for a finite crack in an elastic solid caused by a dilatational wave. Int J Solids Struct 1971;7: 731–50.

[28] Wang C-Y, Achenbach JD. Elastodynamic fundamental solutions for anisotropic solids. Geophys J Int 1994;118:384–92.

[29] Wang C-Y, Achenbach JD, Hirose S. Two-dimensional time domain BEM for scattering of elastic waves in solids of general anisotropy. Int J Solids Struct 1996;33:3843–64.

[30] Wang C-Y. Elastic fields produced by a point source in solid of general anisotropy. J Eng Math 1997;32:41–52.

[31] Zhang Ch, Gross D. On wave propagation in elastic solids with cracks. Southampton UK: Computational Mechanics Publications; 1998.

[32] Zhang Ch, Savaidis A. Time-domain BEM for dynamic crack analysis. Math Comput Simul 1999;50:351–62.

[33] Zhang Ch. Transient elastodynamic antiplane crack analysis of anisotropic solids. Int J Solids Struct 2000;37:6107–30.

[34] Zhang, Ch., Savaidis, A. and Savaidis, G.: Dynamic crack analysis of anistropic solids under impact loading. In: Transactions 16th Int. Conf. on Structural Mechanics in Reactor Technology (Edited by Vernon C. Matzen and C.C. David Tung), Paper #1981. Center for Nuclear Power Plant Structures, Equipment and Piping, North Carolina State University, USA, 2001.

[35] Zhang Ch. A 2-d time-domain BIEM for dynamic analysis of cracked orthotropic solids. Comput Model Eng Sci 2002;3:381–98.

[36] Zhang Ch. A 2-D hypersingular time-domain traction BEM for transient elastodynamic crack analysis. Wave Motion 2002;35:17–40.